
Semi-signed neural fitting for surface reconstruction from unoriented point clouds

Runsong Zhu^{1*} Di Kang² Ka-Hei Hui³ Yue Qian² Xuefei Zhe²

Zhen Dong^{1†} Linchao Bao² Chi-Wing Fu³

¹Wuhan University ²Tencent AI Lab ³The Chinese University of Hong Kong

Abstract

Reconstructing 3D geometry from *unoriented* point clouds can benefit many downstream tasks. Recent methods mostly adopt a neural shape representation with a neural network to represent a signed distance field and fit the point cloud with an unsigned supervision. However, we observe that using unsigned supervision may cause severe ambiguities and often leads to *unexpected* failures such as generating undesired surfaces in free space when reconstructing complex structures and struggle with reconstructing accurate surfaces. To reconstruct a better signed distance field, we propose semi-signed neural fitting (SSN-Fitting), which consists of a semi-signed supervision and a loss-based region sampling strategy. Our key insight is that signed supervision is more informative and regions that are obviously outside the object can be easily determined. Meanwhile, a novel importance sampling is proposed to accelerate the optimization and better reconstruct the fine details. Specifically, we voxelize and partition the object space into *sign-known* and *sign-uncertain* regions, in which different supervisions are applied. Also, we adaptively adjust the sampling rate of each voxel according to the tracked reconstruction loss, so that the network can focus more on the complex under-fitting regions. We conduct extensive experiments to demonstrate that SSN-Fitting achieves state-of-the-art performance under different settings on multiple datasets, including clean, density-varying, and noisy data.

1 Introduction

Surface reconstruction from *unoriented* point clouds is a long-standing fundamental task with many downstream applications in computer vision, computer graphics, and AR/VR. However, due to the unstructured data format of the point clouds, it still remains challenging to reconstruct accurate surfaces for topology-agnostic objects, especially with the presence of noise and density variation.

Among various approaches, implicit methods have gained increasing interest due to the reconstructed smooth and high-fidelity surfaces. In general, they reconstruct surfaces by solving a global (*e.g.*, RBF [8], SPSR [20]), or local (*e.g.*, IMLS [34]) implicit function followed by an isosurface extraction using the marching cubes algorithm [26]. The access to accurate oriented normals plays a crucial role for obtaining good 3D reconstructions in these methods. Unfortunately, it is notoriously hard to compute orientation information from point cloud [6], thus limiting these methods' applicability.

Recently, significant progress [31, 5, 14, 2, 3, 1] has been made in directly optimizing an implicit function (*e.g.* SDF) from unoriented point clouds where only unsigned supervisions can be provided. Among the existing neural methods, SAL [2] is the first to use only unsigned distance as supervision to learn a implicit neural signed distance field, demonstrating successful reconstruction of smooth surfaces while easily missing fine details. IGR [14] proposes to use the unit norm gradient to avoid

*Research done when Runsong Zhu was an intern at Tencent AI Lab.

†Corresponding authors.

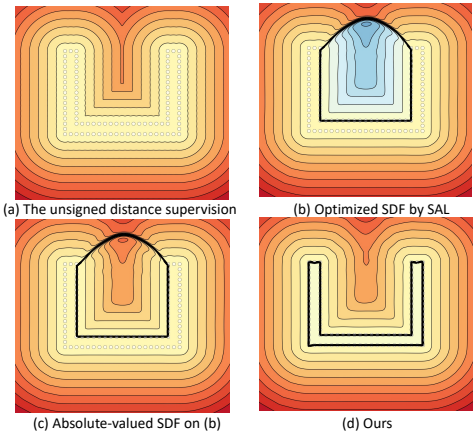


Figure 1: A 2D illustration of the ambiguities in sign-agnostic fitting. Given the unsigned distance field in (a) as constraints, the sign-agnostic method SAL [2] would yield a SDF like (b), whose absolute-valued SDF (c) is quite close to (a), but with undesired resulting surfaces. This is due to the inherent ambiguities caused by lacking sign-related information.

trivial degraded solution and favor natural zero level set surfaces. Further, SALD [3] extends the sign-agnostic optimization to derivative supervision by using unoriented input normals, achieving more accurate surface reconstructions with less sampling complexity[3].

Though substantial improvements have been achieved by the sign-agnostic neural methods [2, 3, 14], there still remain several challenges that prevent them from producing accurate reconstructions. Firstly, using unsigned supervision alone does not provide sufficient guidance so that the network may be stuck into bad local minima that reconstruct weird fake structures, especially when the optimization is done without sufficient regularization. 2D illustration is shown in Fig 1(b). Although the reconstructed surface by unsigned distance supervision [2] is wrong (Fig 1(b) , it indeed satisfies the constraint well in most regions (Fig 1(c)) Secondly, existing methods usually use a fixed sampling strategy throughout the optimization, which often leads to inefficient optimization and thus overly-smoothed surfaces for complex regions as shown in Fig. 2.

To address the above challenges, we first propose a novel *semi-signed fitting module*, which simultaneously provides (i) *a coarse signed supervision*, and (ii) *unsigned supervisions* for different regions determined by our *space partitioning* algorithm automatically. The insight behind this is the signed supervision is more informative and we can apply the signed supervision for the apparently “outside” region to better avoid the ambiguity. Particularly, by collectively adopting the signed supervision with the unsigned supervision to leverage their complementary strengths, it can significantly improve the topological accuracy. Further, to achieve an more effective and more efficient optimization, we design a novel loss-based region sampling strategy by tracking the loss for different regions and adaptively increasing the sampling density of regions with larger losses, thereby focusing the network more on the object details during the optimization, especially after the easy parts are well reconstructed.

In summary, we propose Semi-Signed Neural Fitting (SSN-Fitting) for more accurate and stable surface reconstructions from raw point clouds. Our major contributions are summarized as follows:

- We propose a novel semi-signed learning module, which adaptively adopts signed and unsigned supervisions for different regions determined by our space partition algorithm.
- We introduce a loss-based region sampling, which adaptively adjust the sampling density to account for regions with larger losses, resulting in significantly improved reconstructing quality of complex and fine structures.
- We conduct extensive experiments on clean, density-varying, and noisy datasets, demonstrating the effectiveness, efficiency, and stability of our proposed method.

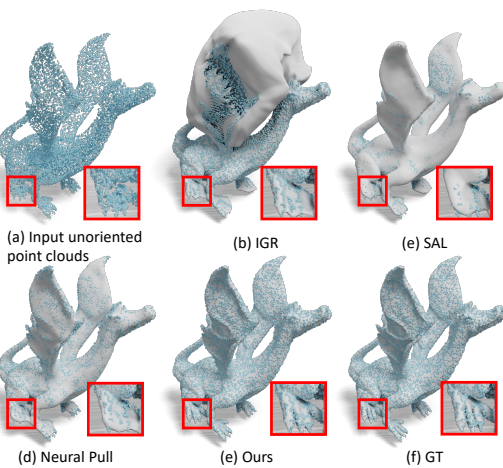


Figure 2: Existing methods [14, 2, 5] utilize a random sampling strategy, hence they have difficulties in reconstructing the fine structures (see the claw of the “dinosaur”). For a better inspection of the reconstruction accuracy, the input point clouds are shown together with the surface results.

2 Related Work

Reconstructing surfaces from unoriented point clouds is a long-standing problem. Here, we review the existing methods from traditional methods to learning-based and neural-optimization-based methods.

Traditional methods. Early methods address the reconstruction task based on either hand-crafted heuristics or numerical optimizations. In particular, some adopt heuristic guidance to progressively build and refine the reconstructed surface, such as growing triangulation [7, 32] and deforming an initial template mesh [22, 33]. Yet, these methods are sensitive to hyperparameters and initialization, requiring careful and time-consuming tuning on *each* point cloud. Some other methods [19, 18, 20, 8, 34, 27] assume that the point cloud comes with a consistently-aligned normal field. However it is highly non-trivial to obtain accurate orientation information for point clouds. The final surface can be reconstructed by solving a Poisson equation [19, 20], or calculating a signed distance function using RBF [8], or moving least squares [34], or Fourier coefficients [18], or wavelets [27].

Learning-based neural implicit methods. Recently, neural implicit function [10, 28, 30] has shown its superiority in representing 3D shapes. With the access to large shape data, such as ShapeNet [9] and Thingi10k [36], [12, 23, 28–30, 4, 13, 17, 25] propose to learn a data prior encoded in a neural implicit function for surface reconstruction from point cloud. The reconstructed surface can then be obtained by applying the trained model to a new point cloud at the inference. To enhance the generalization of the learned prior, [4, 13, 17, 25] propose to learn local priors. However, the priors learned from limited data may lead to overly-smoothed surfaces and the performance may further degrade if the training data does not contain objects similar to the test point cloud.

Fitting-based neural implicit methods. Instead of utilizing a data-driven prior, another works attempts to leverage the neural network as a universal function approximator to solve an optimization for each point cloud input. These methods optimize *one network per object* to implicitly encode a signed distance field (SDF) whose zero-level set represents the reconstructed surface. Some recent works propose to utilize an unsigned supervision to optimize the SDF [2, 3, 14], which are referred as *unsigned* methods in this paper. Other methods [1, 5] project samples in the free space to a zero-level set and compute the distance metric with the input point cloud as the loss function. Note that, we do not classify the Neural-Pull [5] as unsigned method, due to that the surface is not represented as zero-level set which do not satisfy the basic property of SDF. Our work falls into this neural optimization category and extends previous methods with a novel semi-signed supervision and a novel loss-based region sampling strategy so that more complex shapes could be reconstructed better.

3 Method

Given an *unoriented* point cloud \mathcal{P} , our objective is to reconstruct its underlying surface by optimizing a network f_θ parameterized with θ . Specifically, we utilize f_θ to approximate a signed distance field (SDF). Then, we can reconstruct the final surface S_θ by extracting the zero-level set from f_θ :

$$S_\theta = \{p \in \mathbb{R}^3 | f_\theta(p) = 0\}. \quad (1)$$

To obtain the accurate surface, *appropriate supervisions* are required to guide the optimization for the network f_θ . Specifically, the designed supervisions are applied either on the *on-surface* samples (denoted as $p \in \mathcal{P}$) or on the *off-surface* samples (denoted as $q \in \mathbb{R}^3 - \mathcal{P}$) during the optimization process. Using on-surface losses to encourage faithful reconstruction on the sampled surface points while using off-surface losses to regularize the free-space so that unexpected high-frequency fine structures will not be reconstructed.

3.1 Revisiting the existing sign-agnostic optimization

Before presenting our approach in Sec. 3.2-3.3, we first revisit existing supervisions (losses) and discuss their limitations in this subsection. We categorize the existing supervisions into on-surface and off-surface supervisions.

On-surface supervision. The on-surface distance loss $\mathcal{L}_{\text{dist}}^{\text{on}}$ is introduced for on-surface samples (i.e., points $\{p\}$) [14] to encourage the extracted zero-level set from the SDF contains the points. Mathematically, it writes as

$$\mathcal{L}_{\text{dist}}^{\text{on}} = \|f_\theta(p)\|, p \in \mathcal{P}. \quad (2)$$

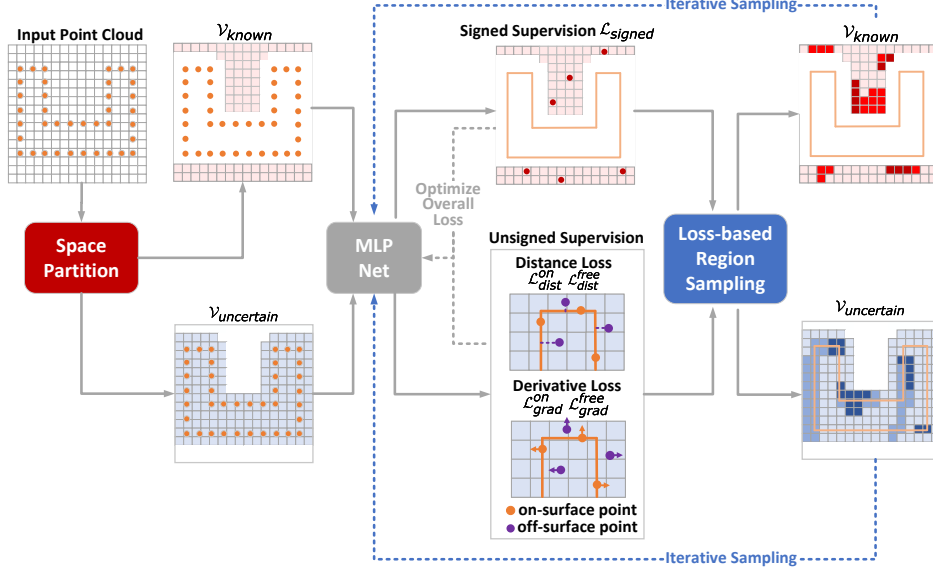


Figure 3: **Overview of our proposed SSN-Fitting method.** Firstly, we partition the object space into “outside” (sign known) regions and “uncertain” (sign uncertain) regions such that we can safely impose signed supervision on the outside regions. This simple signed supervision applied on the outside region effectively avoids reconstructing undesired surfaces, complementing the existing unsigned supervisions (Sec. 3.2). Secondly, we propose a loss-based region sampling strategy to adaptively increase the sampling frequency in complicated regions with larger losses.

And the on-surface unoriented derivative loss $\mathcal{L}_{\text{grad}}^{\text{on}}$ [3] enforces $\nabla f_{\theta}(p)$ to be consistent with the given unoriented surface normal n_p at p :

$$\mathcal{L}_{\text{grad}}^{\text{on}} = \min\{||\nabla f_{\theta}(p) - n_p||, ||\nabla f_{\theta}(p) + n_p||\}, p \in \mathcal{P}, \quad (3)$$

where $\nabla f_{\theta}(p)$ is the derivative of the network in on-surface point p .

Off-surface supervision. Off-surface supervision are applied on off-surface samples $\{q\}$. In details, the unsigned distance supervision $\mathcal{L}_{\text{dist}}^{\text{free}}$ proposed in SAL [2] attempts to supervise the predicted signed distance $f_{\theta}(q)$ with distance d_{GT} which is the distance from q to its closest point in \mathcal{P} :

$$\mathcal{L}_{\text{dist}}^{\text{free}} = \min\{||f_{\theta}(q) - d_{\text{GT}}||, ||f_{\theta}(q) + d_{\text{GT}}||\}, q \in \mathbb{R}^3 - \mathcal{P}. \quad (4)$$

Besides, IGR [14] utilizes the Eikonal regularization [11] for the whole space to encourage a valid SDF with unit-length gradient:

$$\mathcal{L}_{\text{E}} = (\|\nabla f_{\theta}(q) - 1\|)^2. \quad (5)$$

Discussion. Although existing unsigned methods have already achieved promising results, they still struggle to reconstruct the accurate surface for complex region (e.g., thin structure). The signed distance filed optimized by the unsigned distance remain highly under-constrained, this may lead to ambiguity. As shown in Fig. 1(a), for the thin region, the unsigned distance supervision could not provide sufficient information to distinguish whether there is a single plane or two planes. As a result, the neural implicit function may be optimized to a bad local minimum where only a single plane is reconstructed. However, the signed distance function tends to represent a watertight object, thus often resulting in undesired surface in the free space and leading to a large error as in Fig. 1(d).

3.2 Semi-signed optimization module

To alleviate the ambiguity of unsigned supervision, we propose a simple yet effective solution that utilizes part signed information. Intuitively, for a centered watertight shape, we are certain the signs of regions far away from the object are positive since they are *outside* the object. Hence, we introduce an extra signed supervision on the *outside* region, resulting in our *semi-signed optimization module*. To this end, the whole space is firstly partitioned into a *sign-known* region in which the signs of all its points are known (i.e. outside the object) and a *sign-uncertain* region in which the signs of its points cannot be determined beforehand (i.e. regions inside the object and regions close to the surface).

Space partitioning. Space partitioning aims to find the “outside” region $\mathcal{V}_{\text{known}}$ in the unit space for applying signed supervision. Since it is non-trivial to find the accurate boundary of the outside part, we adopt a conservative approach to select the region that is far away from the point clouds as “outside”. Then the complement set of the $\mathcal{V}_{\text{known}}$ is $\mathcal{V}_{\text{uncertain}}$ where the signs of the points inside are uncertain, as shown in Fig. 4. We detail the determination of the $\mathcal{V}_{\text{known}}$ region in the following.

Following the common practice in [14, 2, 3], the input point cloud is first normalized to fit in a cube of range $[-1, +1]^3$. Next, we voxelize the cube space into an N^3 grid, where N is the preset resolution. We mark a voxel as “occupied” if it contains at least one point or its neighbor voxels within a distance threshold R is marked as “occupied” and “empty” otherwise. This verification process is done for all voxels. Since the object is centered, we can choose the voxels at the cube’s boundary and mark them as “empty” as the starting point. Then breadth-first search (BFS) is utilized to find all the voxels connected to it and mark them as “empty”. This set of empty voxels forms our $\mathcal{V}_{\text{known}}$. Pseudo code for this procedure is provided in the supplementary.

Signed supervision in sign-known regions. We enforce the signs predicted by $f_\theta(q), q \in \mathcal{V}_{\text{known}}$ to be positive. This simple yet effective supervision helps the network quickly learn to a coarse shape of the given point clouds. Mathematically, we propose the following loss function:

$$\mathcal{L}_{\text{signed}} = \max(\epsilon - f_\theta(q)), 0, q \in \mathcal{V}_{\text{known}}, \quad (6)$$

where ϵ is a positive margin distance hyper-parameter. This loss only imposes penalization when the predicted SDF value in $\mathcal{V}_{\text{known}}$ is smaller than ϵ , which effectively avoids the ambiguity of the completely unsigned supervision (Fig. 1 (b)). Although we do not use the exact signed distance as the supervision, we observe this positive supervision effectively avoids the generation of fake surfaces in the “outside” region which is under-constrained due to previous sign ambiguity (Fig. 7 (a)).

Unsigned supervision in sign-uncertain region. For the $\mathcal{V}_{\text{uncertain}}$ region, only unsigned supervisions can be used similar to previous methods [14, 2, 3]. Specifically, we adopt both distance loss $\mathcal{L}_{\text{dist}}^{\text{on}}$ (Eq. 2) and derivative loss $\mathcal{L}_{\text{grad}}^{\text{on}}$ (Eq. 3) for on surface points, $\mathcal{L}_{\text{dist}}^{\text{free}}$ (Eq. 4) and Eikonal regularization \mathcal{L}_{E} (Eq. 5) for off surface points.

Considering the point in $\mathcal{V}_{\text{uncertain}}$ region still is under-constrained, we propose a extra unsigned derivative loss Eq. 7) for q as followed:

$$\mathcal{L}_{\text{grad}}^{\text{free}} = \min\{||\nabla f_\theta(q) - n_p||, ||\nabla f_\theta(q) + n_p||\}. \quad (7)$$

According to the following proposition (detailed proof is in the supp.), it is valid to use the normal of the nearest point p (denoted as n_p) in P to approximate the normal of nearest point p' in underlying continuous surface, which equals to the derivative of q , as a supervision for the point q in freespace.

Proposition 1 Given a random point q in the free space and its closet point on the underlying surface is p' , then we have $\frac{\nabla f(p')}{\|\nabla f(p')\|} = \frac{\nabla f(q)}{\|\nabla f(q)\|}$ when derivative exists almost everywhere for f .

We notice the proposed derivative supervision in freespace can accelerate the fitting process of thin structures (see Fig. 11). Intuitively, when the reconstructed surface is optimized to a rough shape to the thin structure, the distance supervision ($\mathcal{L}_{\text{dist}}^{\text{on}}$ and $\mathcal{L}_{\text{dist}}^{\text{off}}$) will be very small. In addition, the existing derivative supervision for on-surface points, even could be near to zero as shown in Fig. 5. Fortunately, the proposed derivative supervision in free space may provide a extra strong guild information and hence accelerating the process.

Overall optimization objective. The overall loss is the weighted sum of the aforementioned loss terms as

$$\mathcal{L} = w_1 \mathcal{L}_{\text{dist}}^{\text{on}} + w_2 \mathcal{L}_{\text{dist}}^{\text{free}} + w_3 \mathcal{L}_{\text{grad}}^{\text{on}} + w_4 \mathcal{L}_{\text{grad}}^{\text{free}} + w_5 \mathcal{L}_{\text{E}} + w_6 \mathcal{L}_{\text{signed}}, \quad (8)$$

where $\{w_i\}$ are weights of each loss term.

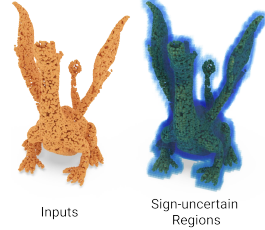


Figure 4: Space partitioning.

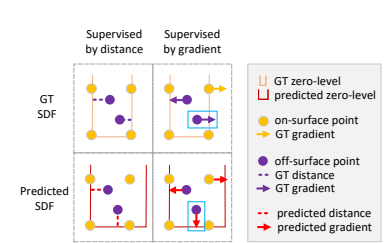


Figure 5: Derivative supervision in freespace.

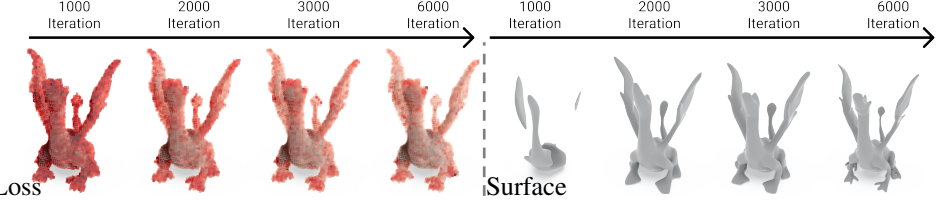


Figure 6: Visualization of the tracked moving average loss ($\mathcal{M}_{\text{grad}}^{i-\text{on}}$) in every voxel throughout the optimization. More red colors indicate higher loss values. Overall, all the tracked moving average losses are getting smaller. And the losses in easier regions decrease faster than more complicated regions, resulting in lower sampling probabilities as the fitting going on. With our loss-based per-region sampling strategy, the network can focus more on the hard regions.

3.3 Loss-based per-region sampling

We propose to sample more points for optimization if a region has larger tracked loss, which can be regarded as a new variant of importance sampling. This strategy brings two main benefits: 1) it can facilitate the reconstruction of fine details in complex regions since regions have more details are normally harder to fit, and avoid creating undesired surface in freespace. 2) it can accelerate the training process by reducing the computation spent on low complexity regions. Concretely, our strategy consists of two main steps, i.e., region-wise loss tracking and adaptive sampling.

Region-wise loss tracking. We consider all five major loss terms ($\mathcal{L}_{\text{dist}}^{\text{on}}, \mathcal{L}_{\text{dist}}^{\text{off}}, \mathcal{L}_{\text{grad}}^{\text{on}}, \mathcal{L}_{\text{grad}}^{\text{off}}, \mathcal{L}_{\text{signed}}$). Taking $\mathcal{L}_{\text{dist}}^{\text{on}}$ for example, we track the running mean loss of all applicable voxels \mathcal{V}^i (occupied voxels for $\mathcal{L}_{\text{dist}}^{\text{on}}$) as follows.

$$\mathcal{M}_{\text{dist}}^{i-\text{on}} = (1 - \alpha) \times \mathcal{M}_{\text{dist}}^{i-\text{on}} + \alpha \times \mathcal{L}_{\text{dist}}^{i-\text{on}}, \quad (9)$$

where $\mathcal{L}_{\text{dist}}^{i-\text{on}}$ is the loss of voxel i in the current iteration, $\mathcal{M}_{\text{dist}}^{i-\text{on}}$ is the tracked running mean loss, and α is the momentum set to 0.1 empirically. Similarly, we can track the other losses denoted as $\mathcal{M}_{\text{grad}}^{i-\text{on}}, \mathcal{M}_{\text{dist}}^{i-\text{off}}, \mathcal{M}_{\text{grad}}^{i-\text{off}},$ and $\mathcal{M}_{\text{signed}}^i$ respectively. Note that different losses are applied on different regions (voxels). Please refer to the supplementary for more details.

Adaptive sampling. With the tracked running means, we can perform a two-step sampling for each loss: 1) adaptively sample a set of voxels based on the previous region losses, and then 2) sample points within each region (voxels). For the first step, we sample a set of voxels, where each voxel \mathcal{V}^i is assigned with a sampling probability $p_{\text{type}-i}^i$ proportional to the tracked moving average loss:

$$p_{\text{type}-i} = \frac{\mathcal{M}_{\text{type}-i}}{\sum_j \mathcal{M}_{\text{type}-j}}, \quad (10)$$

where $\mathcal{M}_{\text{type}-j} \in \{\mathcal{M}_{\text{dist}}^{j-\text{on}}, \mathcal{M}_{\text{grad}}^{j-\text{on}}, \mathcal{M}_{\text{dist}}^{j-\text{off}}, \mathcal{M}_{\text{grad}}^{j-\text{off}}, \mathcal{M}_{\text{signed}}^j\}$. Then, we apply different procedures to obtain the final point samples according the loss types. For the off-surface losses ($\mathcal{L}_{\text{dist}}^{\text{off}}, \mathcal{L}_{\text{grad}}^{\text{off}}$) and the signed loss $\mathcal{L}_{\text{signed}}$, similar to [14], the points are sampled from two Gaussian distributions whose means are both the voxel center location while their standard derivations are $\sigma_1 = \frac{1}{N}$ and $\sigma_2 = \frac{1}{2 \times N}$ respectively. For on-surface losses ($\mathcal{L}_{\text{dist}}^{\text{on}}$ and $\mathcal{L}_{\text{grad}}^{\text{on}}$), we query the k-nearest neighbor (k-NN) input points to the voxel center. Note that a small Gaussian noise is added to the center location before k-NN so that different points can be sampled in different iterations. We provide a visualization on the sampling probabilities of the voxels in Fig. 6. Note that our strategy tends to sample regions containing complex structures and fine details more often. The ablation study in Sec. 4.5 (Fig. 10) shows that using our proposed sampling makes the network fit the complex regions better, demonstrating the effectiveness of our sampling strategy. More details is in supp.

4 Results

4.1 Experiment setting

Datasets. To test the stability of the proposed method, we conduct comprehensive comparisons with other methods on three different types of datasets, including (i) clean point clouds, including 100 noise-free and uniformly-sampled point clouds from various CAD models released by Points2surf [12]

Table 1: The quantitative results under different types of input point clouds (clean data, density-varying data, noisy data). We report the averaged value on each dataset of the F-score under the 1% threshold F-score, L1 Chamfer Distance (CD (L1)) and Normal Consistency (NC). N-P is short for Neural-Pull [5].

| Methods | Clean data | | | Density-varying data | | | Noisy data | | |
|-----------|--------------|--------------|--------------|----------------------|--------------|--------------|--------------|--------------|--------------|
| | F-score | CD (L1) | NC | F-score | CD (L1) | NC | F-score | CD (L1) | NC |
| SAP [31] | 0.660 | 1.368 | 0.915 | 0.889 | 0.658 | 0.932 | 0.58 | 1.128 | 0.693 |
| SPSR [20] | 0.557 | 2.774 | 0.904 | 0.789 | 2.007 | 0.938 | 0.723 | 2.216 | 0.833 |
| IMLS [25] | 0.626 | 1.245 | 0.923 | 0.83 | 0.715 | 0.925 | 0.583 | 1.205 | 0.879 |
| N-P [5] | 0.370 | 2.071 | 0.912 | 0.397 | 1.359 | 0.945 | 0.257 | 2.027 | 0.901 |
| SAL [2] | 0.353 | 3.499 | 0.878 | 0.522 | 1.667 | 0.919 | 0.394 | 2.083 | 0.922 |
| IGR [14] | 0.551 | 4.429 | 0.891 | 0.714 | 7.316 | 0.918 | 0.697 | 3.48 | 0.889 |
| Our | 0.669 | 1.215 | 0.934 | 0.919 | 0.557 | 0.963 | 0.731 | 1.044 | 0.952 |

(a subset of ABC dataset [21]); (ii) point clouds in varying sampling density, including 32 shapes with two different types of density variations (gradient and striped) from PCPNet [15]; and (iii) noisy point clouds with different levels (i.e. low, med and high) of noise, including 57 shapes from PCPNet [15].

Evaluation metrics. We report L1-based Chamfer Distance (denoted as “CD (L1)”), Normal Consistency (“NC”), and F1-score with default threshold 1% following SAP [31] (“F-score”) between reconstructed surface and GT. Following SAP [31], we use the same procedure as SAP [31] to calculate the metrics (detail description is in supp).

Baselines. We consider three types of methods for comparison: (i) a classic traditional method, Screened Poisson Surface Reconstruction (SPSR) [20]; (ii) a learning-based method, IMLSNet [25]; and (iii) four optimization-based methods, including IGR [14], SAL [2], Neural-Pull [5], and SAP [31]. The results of IMLSNet [25] (denoted as “IMLS” in the following tables and figures) are calculated based on their officially released pre-trained model. For the other baselines (IGR [14], SAL [2], Neural-Pull [5] (denoted as “N-P”) and SAP [31]), we report the results optimized by their officially released code. The normal inputs of our method and SPSR [20] are estimated from a state-of-the-art method AdaFit[37]. Considering that SPSR [20] requires consistently oriented normals, we use minimum spanning tree [35] to propagate the normal orientations [16].

Implementation details. Following [2, 3, 14, 5], we overfit the network for every input point cloud. For the clean data and density varying data, the weight parameter are $w_i = \{40, 20, 1, 1, 1, 10\}$ in Eq. 8. For the noisy data, the weight parameter are adjusted to $w_i = \{20, 10, 20, 10, 1, 10\}$ to rely less on distance losses ($\mathcal{L}_{\text{dist}}$, $\mathcal{L}_{\text{dist}}^{\text{free}}$) and rely more on gradient losses ($\mathcal{L}_{\text{grad}}$, $\mathcal{L}_{\text{grad}}^{\text{free}}$).

4.2 Results on clean data

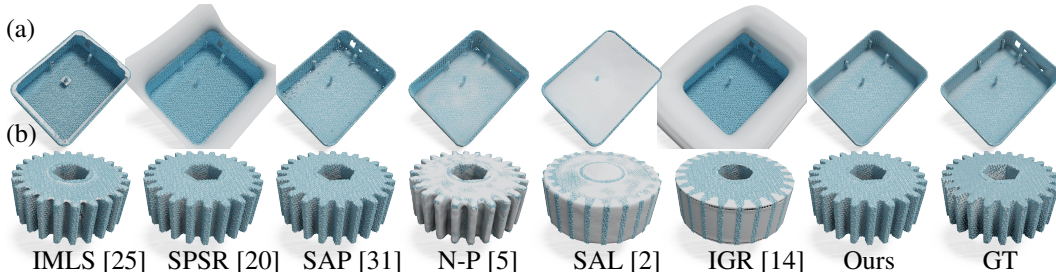


Figure 7: Visual comparison of reconstructions from clean data. The result reconstructed by IGR [14] and SAL [2] is over-smooth and there exists undesired surface in freespace. Although SAP [31] and N-P [5] can reconstruct more accurate surfaces, the results contain many artifacts. SPSR [20] and IMLS [25] yield more accurate surfaces in planar regions while creating many artifacts around sharp edges. Our method can reconstruct accurate and smooth surfaces.

Quantitative results of different methods on the clean data are shown in Tab. 1. Overall, our method achieves the best results on all the metrics (*i.e.*, F-score, CD (L1), NC). Fig. 7 shows the visual results on clean data. In general, shapes reconstructed by our method better preserve the sharp edges and produce less high-frequency bumps in the plane region. Note that SAP [31] results contain many

artifacts although it achieves very good quantitative results. The results from other optimization-based neural methods (IGR [14], SAL [2], Neural-Pull [5]) usually lose many details, resulting in overly-smoothed reconstructions, and occasionally create undesired false surfaces. As for SPSR [20], it heavily suffers from incorrectly estimated normal orientations in complex regions even on the clean data. IMLS [25] reconstruct the accurate surface in simple region (e.g. plane region), but it suffer the inaccurate prediction on the sharp region.

4.3 Results on varying-density data

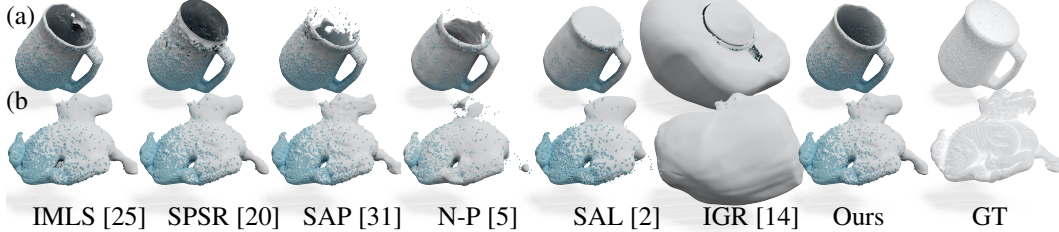


Figure 8: Visual comparison of reconstructions from varying-density data. IGR [14] and SAL [2] may create undesired surfaces while N-P [5], SAP [31] and IMLS [25] are very sensitive to density changes, resulting many small holes. SPSR [20] fails to reconstruct the surfaces for the column shape due to the inaccurate orientation calculation of normals. Note that the GT are uniformly sampled point clouds provided by the PCPNet [15] dataset.

Considering that the obtained point cloud data are commonly non-uniform, we show experimental results on point clouds with varying density from PCPNet dataset [15]. As shown in Tab. 1, our method performs best on all three metrics. Our method reconstructs more accurate details, which is supported by the best NC score in Tab. 1 and the visual comparisons in Fig. 8. Our method also produces more complete surfaces and sharp edges when handling point clouds in varying density. In comparison, IGR [14] and SAL [2] reconstruct overly-smoothed surface and sometimes generate undesired false surfaces in the free space. As a contrast, the results from other methods (SPSR [20], IMLS [25], Neural-pull [5] and SAP [31]) contain many holes and sometimes fail to reconstruct the sparse regions, especially the results of Neural-pull [5] and SAP [31] in Fig. 8.

4.4 Results on noisy data

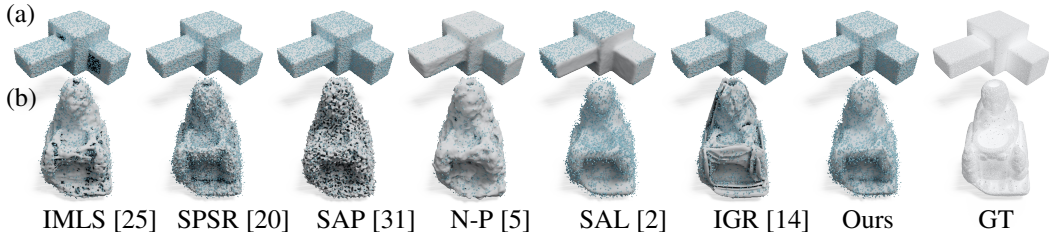


Figure 9: Visual comparison of reconstructions from noisy data. As expected, SAP[31], IGR [14] and N-P [5] are very sensitive to noises, since they do not apply any smooth constraints (*i.e.* normals) and thus would treat noise points as surface details. Compared with IGR [14], SAL [2] is more robust to noises as it tends to yield over-smooth reconstructions. The learning based method (*i.e.* IMLS [25]) suffers from the generalization ability of the network, which would even create undesired artifacts in planar regions (see the example in the first row).

To test the robustness of our method on noisy data, we conduct the experiments on point clouds containing different levels (*i.e.*, low-level, med-level, high-level) of noise from PCPNet [15]. Our method significantly outperforms the baseline methods on all the metrics quantitatively (Tab. 1). Visual comparisons in Fig. 9 have validated this. As expected, SAP[31], IGR [14] and N-P [5] fit the surface details with the noise point with no differences. Since there is no any smooth constrain (*i.e.* normal information) in these methods, they are very sensitive to the noise. Compared with IGR [14], the SAL [2] is more robust to noise due to they do not fitting the noisy point clouds. The learning based method (*i.e.* IMLS [25]) suffer from the generalization of network, which even create

Table 2: The quantitative results for the ablation study.

| | Clean data | | | Density-varying data | | | Noisy data | | |
|-----------------------------|------------|-------|-------|----------------------|-------|-------|------------|-------|-------|
| | F-score | CD1 | NC | F-score | CD1 | NC | F-score | CD1 | NC |
| Full | 0.669 | 1.215 | 0.934 | 0.919 | 0.557 | 0.963 | 0.731 | 1.044 | 0.952 |
| w/o SS | 0.657 | 1.215 | 0.932 | 0.906 | 0.577 | 0.948 | 0.701 | 2.053 | 0.945 |
| w/o LRS | 0.650 | 1.558 | 0.933 | 0.917 | 0.586 | 0.960 | 0.706 | 1.325 | 0.949 |
| Ours (w/ LRS) | 0.669 | 1.215 | 0.934 | 0.919 | 0.557 | 0.963 | 0.731 | 1.044 | 0.952 |
| Focal loss ($\gamma=1$) | 0.561 | 2.214 | 0.927 | 0.773 | 1.795 | 0.942 | 0.658 | 1.503 | 0.947 |
| Focal loss ($\gamma=0.5$) | 0.621 | 1.882 | 0.933 | 0.87 | 0.973 | 0.947 | 0.667 | 2.021 | 0.943 |

undesired artifacts in plane region, as shown in Fig 9 (b). Our method and SPSR [20] benefit from the derivative constrain, which can effectively avoid over-fitting to the noise.

4.5 Ablation study

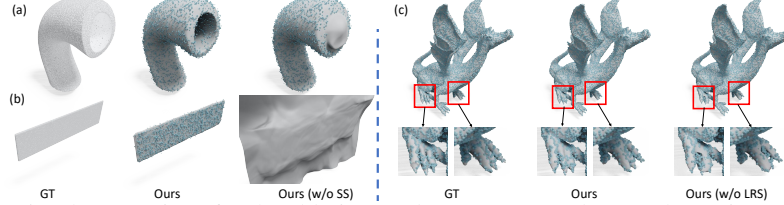


Figure 10: Visual comparison for the ablation study. More examples are shown in our supplementary.

Semi-signed (SS) optimization module. We conduct experiments to show the effectiveness of SS optimization module in Tab. 2 and Fig. 10 (a),(b). We can see the proposed SS effectively avoids the undesired surfaces in the free space. Besides, we especially conduct the experiment on the thin structure for the proposed derivative supervision in free space. We compare optimization with and without derivative supervision in the free space in Fig. 11. Introducing this supervision accelerates the fitting process (Fig. 11a) and reconstructs the thin structure better (Fig. 11b).

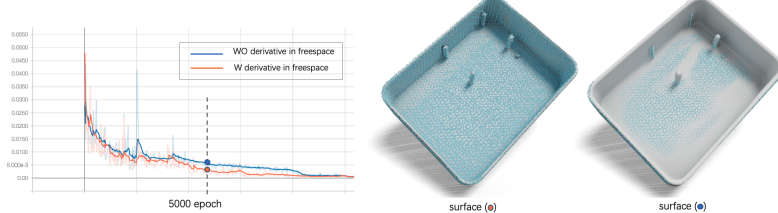


Figure 11: Ablation study on derivative supervision in free space. On-surface loss curves are plotted and the reconstructed surfaces after 5000 iteration of optimization are compared. More accurate result for the thin structure is achieved with the proposed derivative supervision in free space.

Loss-based per-region sampling. We conduct ablative experiments to show the effectiveness of the loss-based per-region sampling (LRS) in Tab. 2 (1st & 3rd rows). One representative example is selected from Thing10k [36] for better visual illustration (Fig. 10c). We can see LRS significantly improves the quality of reconstructed results, especially for the complex region.

Alternative method of loss-based per-region sampling. There are other alternatives that can achieve similar effect to our proposed loss-based per-region sampling. Here we compare with focal loss [24] since it also pays more attention to the less well reconstructed regions. In this experiment, our sampling strategy is replaced by $\mathcal{L}_{\text{weighed}} = \mathcal{L}^\gamma \cdot \mathcal{L}$. Quantitative results in Tab. 2 (bottom) show that our sampling strategy achieves better performance, than focal loss [24], especially on noisy data.

5 Conclusion and Limitation

We find network optimized using only unsigned supervision occasionally creates fake surfaces in free space and often struggles with reconstructing accurate surface. So we propose a semi-signed optimization module to avoid creating fake surfaces in free space and adopt a loss-based per-region sampling to improve the detail reconstruction. Our SSN-Fitting method has achieved largely improved performance on multiple datasets, including clean point clouds, density-varying point clouds, and noisy point clouds. One limitation of our method is it can not handle point clouds with large missing parts (i.e. partial scan) since the calculation of the “outside” region is highly unreliable.

References

- [1] Atzmon, M., Haim, N., Yariv, L., Israelov, O., Maron, H., Lipman, Y.: Controlling neural level sets. *Advances in Neural Information Processing Systems* **32** (2019)
- [2] Atzmon, M., Lipman, Y.: Sal: Sign agnostic learning of shapes from raw data. In: *Proceedings of the IEEE/CVF Conference on Computer Vision and Pattern Recognition*. pp. 2565–2574 (2020)
- [3] Atzmon, M., Lipman, Y.: Sald: Sign agnostic learning with derivatives. *arXiv preprint arXiv:2006.05400* (2020)
- [4] Badki, A., Gallo, O., Kautz, J., Sen, P.: Meshlet priors for 3d mesh reconstruction. In: *IEEE Conf. on Computer Vision and Pattern Recognition*. pp. 2849–2858 (2020)
- [5] Baorui, M., Zhizhong, H., Yu-shen, L., Matthias, Z.: Neural-pull: Learning signed distance functions from point clouds by learning to pull space onto surfaces. In: *International Conference on Machine Learning (ICML)* (2021)
- [6] Berger, M., Tagliasacchi, A., Seversky, L.M., Alliez, P., Guennebaud, G., Levine, J.A., Sharf, A., Silva, C.T.: A survey of surface reconstruction from point clouds. In: *Computer Graphics Forum*. vol. 36, pp. 301–329. Wiley Online Library (2017)
- [7] Bernardini, F., Mittleman, J., Rushmeier, H., Silva, C., Taubin, G.: The ball-pivoting algorithm for surface reconstruction. *IEEE Trans. Vis. & Comp. Graphics* **5**(4), 349–359 (1999)
- [8] Carr, J.C., Beatson, R.K., Cherrie, J.B., Mitchell, T.J., Fright, W.R., McCallum, B.C., Evans, T.R.: Reconstruction and representation of 3d objects with radial basis functions. In: *Proceedings of the 28th annual conference on Computer graphics and interactive techniques*. pp. 67–76 (2001)
- [9] Chang, A.X., Funkhouser, T.A., Guibas, L.J., Hanrahan, P., Huang, Q., Li, Z., Savarese, S., Savva, M., Song, S., Su, H., Xiao, J., Yi, L., Yu, F.: ShapeNet: An information-rich 3D model repository. *arXiv preprint arXiv:1512.03012* (2015)
- [10] Chen, Z., Zhang, H.: Learning implicit fields for generative shape modeling. In: *IEEE Conf. on Computer Vision and Pattern Recognition*. pp. 5939–5948 (2019)
- [11] Crandall, M.G., Lions, P.L.: Viscosity solutions of hamilton-jacobi equations. *Transactions of the American mathematical society* **277**(1), 1–42 (1983)
- [12] Erler, P., Guerrero, P., Ohrhallinger, S., Mitra, N.J., Wimmer, M.: Points2surf learning implicit surfaces from point clouds. In: *European Conference on Computer Vision*. pp. 108–124 (2020)
- [13] Genova, K., Cole, F., Sud, A., Sarna, A., Funkhouser, T.: Local deep implicit functions for 3d shape. In: *IEEE Conf. on Computer Vision and Pattern Recognition*. pp. 4857–4866 (2020)
- [14] Gropp, A., Yariv, L., Haim, N., Atzmon, M., Lipman, Y.: Implicit geometric regularization for learning shapes. In: *Proceedings of Machine Learning and Systems 2020*, pp. 3569–3579 (2020)
- [15] Guerrero, P., Kleiman, Y., Ovsjanikov, M., Mitra, N.J.: Pcpnet learning local shape properties from raw point clouds. In: *Computer Graphics Forum*. vol. 37, pp. 75–85. Wiley Online Library (2018)
- [16] Hoppe, H., DeRose, T., Duchamp, T., McDonald, J., Stuetzle, W.: Surface reconstruction from unorganized points. In: *Proceedings of the 19th annual conference on Computer graphics and interactive techniques*. pp. 71–78 (1992)
- [17] Jiang, C., Sud, A., Makadia, A., Huang, J., Nießner, M., Funkhouser, T., et al.: Local implicit grid representations for 3d scenes. In: *IEEE Conf. on Computer Vision and Pattern Recognition*. pp. 6001–6010 (2020)
- [18] Kazhdan, M.: Reconstruction of solid models from oriented point sets. In: *Proceedings of the third Eurographics symposium on Geometry processing*. pp. 73–es (2005)
- [19] Kazhdan, M., Bolitho, M., Hoppe, H.: Poisson surface reconstruction. In: *Proceedings of the fourth Eurographics symposium on Geometry processing*. vol. 7 (2006)
- [20] Kazhdan, M., Hoppe, H.: Screened poisson surface reconstruction. *Proc. of SIGGRAPH* **32**(3), 1–13 (2013)

[21] Koch, S., Matveev, A., Jiang, Z., Williams, F., Artemov, A., Burnaev, E., Alexa, M., Zorin, D., Panozzo, D.: Abc: A big cad model dataset for geometric deep learning. In: Proceedings of the IEEE/CVF Conference on Computer Vision and Pattern Recognition. pp. 9601–9611 (2019)

[22] Li, G., Liu, L., Zheng, H., Mitra, N.J.: Analysis, reconstruction and manipulation using arterial snakes. ACM Transactions on Graphics (SIGGRAPH Asia) **29**(6), 152 (2010)

[23] Liao, Y., Donne, S., Geiger, A.: Deep marching cubes: Learning explicit surface representations. In: IEEE Conf. on Computer Vision and Pattern Recognition. pp. 2916–2925 (2018)

[24] Lin, T.Y., Goyal, P., Girshick, R., He, K., Dollár, P.: Focal loss for dense object detection. In: Proceedings of the IEEE international conference on computer vision. pp. 2980–2988 (2017)

[25] Liu, S.L., Guo, H.X., Pan, H., Wang, P.S., Tong, X., Liu, Y.: Deep implicit moving least-squares functions for 3d reconstruction. In: Proceedings of the IEEE/CVF Conference on Computer Vision and Pattern Recognition. pp. 1788–1797 (2021)

[26] Lorensen, W.E., Cline, H.E.: Marching cubes: A high resolution 3d surface construction algorithm. ACM siggraph computer graphics **21**(4), 163–169 (1987)

[27] Manson, J., Petrova, G., Schaefer, S.: Streaming surface reconstruction using wavelets. In: Computer Graphics Forum. vol. 27, pp. 1411–1420 (2008)

[28] Mescheder, L., Oechsle, M., Niemeyer, M., Nowozin, S., Geiger, A.: Occupancy networks: Learning 3d reconstruction in function space. In: IEEE Conf. on Computer Vision and Pattern Recognition. pp. 4460–4470 (2019)

[29] Mi, Z., Luo, Y., Tao, W.: Ssrnet: Scalable 3d surface reconstruction network. In: IEEE Conf. on Computer Vision and Pattern Recognition. pp. 970–979 (2020)

[30] Park, J.J., Florence, P., Straub, J., Newcombe, R., Lovegrove, S.: DeepSDF: Learning continuous signed distance functions for shape representation. In: IEEE Conf. on Computer Vision and Pattern Recognition. pp. 165–174 (2019)

[31] Peng, S., Jiang, C., Liao, Y., Niemeyer, M., Pollefeys, M., Geiger, A.: Shape as points: A differentiable poisson solver. Advances in Neural Information Processing Systems **34** (2021)

[32] Scheidegger, C.E., Fleishman, S., Silva, C.T.: Triangulating point set surfaces with bounded error. In: Symp. on Geom. Proc. pp. 63–72 (2005)

[33] Sharf, A., Lewiner, T., Shamir, A., Kobbelt, L., Cohen-Or, D.: Competing fronts for coarse–to–fine surface reconstruction. In: Computer Graphics Forum. vol. 25, pp. 389–398 (2006)

[34] Shen, C., O’Brien, J.F., Shewchuk, J.R.: Interpolating and approximating implicit surfaces from polygon soup. In: ACM SIGGRAPH 2004 Papers, pp. 896–904 (2004)

[35] Zhou, Q.Y., Park, J., Koltun, V.: Open3d: A modern library for 3d data processing. arXiv preprint arXiv:1801.09847 (2018)

[36] Zhou, Q., Jacobson, A.: Thingi10k: A dataset of 10,000 3d-printing models. arXiv preprint arXiv:1605.04797 (2016)

[37] Zhu, R., Liu, Y., Dong, Z., Wang, Y., Jiang, T., Wang, W., Yang, B.: Adafit: Rethinking learning-based normal estimation on point clouds. In: Proceedings of the IEEE/CVF International Conference on Computer Vision. pp. 6118–6127 (2021)

Supplementary Materials

A Space partition algorithm details (pseudo code)

Here, we provide the pseudo code for finding the “outside” region (Sec. 3.2 in main text) from occupied voxels in Algo. 1.

Algorithm 1: Space Partitioning (Python style)

Input :3D array V_{occ} , indicating if a voxel is occupied
Output :3D array V_{outside} , indicating if a voxel is outside the object for sure
// shape: $N \times N \times N$

```

1 Initialize a visited list  $V_v$  with 0;
2 outside = { };
    // Step 1: find all empty voxels on the six faces of the cube and
    // label them as “outside”
    // test voxels on two opposite faces of the cube
3 for  $i$  in  $\{1, N\}$  do
4     for  $j \leftarrow 1$  to  $N$  do
5         for  $k \leftarrow 1$  to  $N$  do
6             if  $V_{\text{occ}}[i, j, k] == 0$  and  $V_v[i, j, k] == 0$  then
7                  $V_{\text{outside}}[i, j, k] = 1$ ;
8                 outside.append([i,j,k]);
9             end
10             $V_v[i, j, k] = 1$ ;
11        end
12    end
13 end
    // test the other two sets of opposite faces similarly
14    :
    // Step 2: a BFS-like procedure to recursively find all “outside”
    // voxel connected to the initial outside voxels on the six faces
15 offset = {[1, 0, 0], [-1, 0, 0], [0, 1, 0], [0, -1, 0], [0, 0, 1], [0, 0, -1]};
16 while index < outside.size() do
17     cur_pos = outside[index];
18     for  $i \leftarrow 1$  to 6 do
        // test all six faces
19         neighbor_pos = {cur_pos[1] + offset[i][1], cur_pos[2] + offset[i][2], cur_pos[3] +
            offset[i][3]};
20         if check_valid(neighbor_pos) and  $V_{\text{occ}}[\text{neighbor\_pos}] == 0$  and
             $V_v[\text{neighbor\_pos}] == 0$  then
            // if this is a valid && occupied && not visited position
21              $V_{\text{outside}}[\text{neighbor\_pos}] = 1$ ;
             // add connected outside voxel
22             outside.append(neighbor_pos);
23         end
24          $V_v[\text{neighbor\_pos}] = 1$ ;
25         index = index + 1
26     end
27 end
28 return  $V_{\text{outside}}$ 

```

B Proof for proposition

Proposition 2 Given a random point q in the free space and its closet point on the underlying surface p' , then we have $\frac{\nabla f(p')}{\|\nabla f(p')\|} = \frac{\nabla f(q)}{\|\nabla f(q)\|}$ when derivative exists almost everywhere for f .

We first consider point q is inside the underlying shape, which means $f(q) < 0$.

(1) Firstly, we prove the following proposition:

$$\frac{\nabla f(p')}{\|\nabla f(p')\|} = \frac{q - p'}{\|q - p'\|}, \quad (11)$$

where $\|\cdot\|$ is L2 norm. Since p' is q 's closest point on the underlying surface defined by $f(x) = 0$, $p' = \operatorname{argmin}_x \|x - q\|$ s.t. $f(x) = 0$. And the corresponding Lagrange function is:

$$L(x) = \|x - q\| + \lambda f(x), \quad (12)$$

whose gradient can be calculated as:

$$\nabla_{(p', \lambda)} L = \left(\frac{-(q - p')}{\|q - p'\|} + \lambda \nabla f(p'), f(p') \right), \quad (13)$$

Let $\frac{-(q - p')}{\|q - p'\|} + \lambda \nabla f(p') = 0$, and we get $\nabla f(p') = \lambda \frac{q - p'}{\|q - p'\|}$. Hence we know that $\nabla f(p')$ is collinear to vector $(q - p')$. Considering the gradient denotes the direction of greatest increase of function, we have $\frac{\nabla f(p')}{\|\nabla f(p')\|} = \frac{q - p'}{\|q - p'\|}$.

(2) Then we can prove:

$$\frac{\nabla f(q)}{\|\nabla f(q)\|} = \frac{q - p'}{\|q - p'\|} = \frac{\nabla f(p')}{\|\nabla f(p')\|} \quad (14)$$

According the definition of directional derivative

$$\nabla_v f(x) = \lim_{h \rightarrow 0} \frac{f(x + hv) - f(x)}{h}, \quad (15)$$

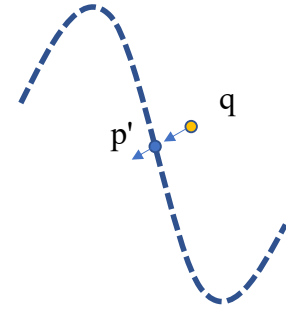
where v is the given unit vector. The relationship between gradient and directional derivative on point q can be wrote as $\frac{\nabla f(q)}{\|\nabla f(q)\|} = \operatorname{argmax}_v \nabla_v f(q)$ and $\|\nabla f(q)\| = \max_v \nabla_v f(q)$.

Due to that the signed distance function should satisfy $\|\nabla f(q)\| = 1$, we can know that the directional derivative always satisfy $\nabla_v f(q) \leq \|\nabla f(q)\| = 1$ for any direction v . Moreover, by definition, $\nabla_v f(q)$ can be expressed as $\nabla_v f(q) = \lim_{h \rightarrow 0} \frac{f(q + hv) - f(q)}{h}$.

Let us consider the specific direction $v' = \frac{q - p'}{\|q - p'\|}$ and let $q^* = q + hv'$. We also denote $p'' = \operatorname{argmin}_v \|q^* - p\|$. We can prove that $p'' = p'$ by contradiction, i.e. if $p'' \neq p'$, then $\|q^* - p''\| < \|q^* - p\|$. We add the same value on each side of the inequality, $\|q^* - q\| + \|q^* - p''\| < \|q^* - q\| + \|q^* - p'\| = \|q - p'\|$ since q^* locates in the line segment (q, p') . However, $\|q^* - q\| + \|q^* - p''\| \geq \|q - p''\| > \|q - p'\|$ which leads to contradiction. Therefore, $p'' = p'$.

Thus, $\nabla_{v'} f(q) = \lim_{h \rightarrow 0} \frac{f(q^*) - f(q)}{h} = \lim_{h \rightarrow 0} \frac{-1 * \|q^* - p'\| - (-1) * \|q - p'\|}{h} = 1$. Hence, the direction v' yields $\operatorname{argmax}_v \nabla_v f(q)$. So, $\frac{\nabla f(q)}{\|\nabla f(q)\|} = \frac{q - p'}{\|q - p'\|}$.

In the meantime, if q is outside of the shape, then it can be proved that $\frac{\nabla f(p)}{\|\nabla f(p)\|} = \frac{\nabla f(q)}{\|\nabla f(q)\|} = \frac{-(q - p')}{\|q - p'\|}$ by similar way.



C Loss-based per-region sampling details

Different losses (i.e. $\mathcal{L}_{\text{dist}}^{\text{on}}$, $\mathcal{L}_{\text{dist}}^{\text{off}}$, $\mathcal{L}_{\text{grad}}^{\text{on}}$, $\mathcal{L}_{\text{grad}}^{\text{off}}$, $\mathcal{L}_{\text{signed}}$) are applicable on different voxels (Sec. 3.3 in main text). Specifically, we track $\mathcal{L}_{\text{dist}}^{\text{on}}$ and $\mathcal{L}_{\text{grad}}^{\text{on}}$ for the voxels which contain points. We track $\mathcal{L}_{\text{dist}}^{\text{off}}$ and $\mathcal{L}_{\text{grad}}^{\text{off}}$ for all the voxels in region $\mathcal{V}_{\text{uncertain}}$. We track $\mathcal{L}_{\text{signed}}$ for all the voxels in region $\mathcal{V}_{\text{known}}$.

D Experimental details

Optimization setting As shown in Tab. 1, we optimize our method for 20,000 epoch for each shape and the same epoch for IGR [14]. We optimize the SAL [2] for 4,000 epoch to keep similar optimizing time to our method and IGR [2] for a fair comparison. For Neural-Pull [5], we optimize the neural network to the maximum epoch (40,000) in their official code. For SAP [31], We just follow the provided optimization-based setting to report the results.

Table 3: The optimization epoch & approximate time for different optimization-based neural method.

| Method | Our | IGR [14] | SAL [2] | Neural-Pull [5] |
|------------------|--------|----------|---------|-----------------|
| Epoch | 20,000 | 20,000 | 4,000 | 40,000 |
| Opt. time (min.) | ~ 22 | ~ 30 | ~ 26 | ~ 15 |

Evaluation metrics We follow the same procedure as in SAP [31] to calculate the metrics, including L1-based Chamfer Distance (denoted as “CD (L1)”, Normal Consistency (“NC”), and F1-score with default threshold 1% in main text Sec. 4.1. Specifically, for the clean data, we randomly sample 40,000 points each on the reconstructed mesh and the ground-truth mesh respectively to calculate the aforementioned metrics. For the density-varying data and noisy data, we directly use the provided point cloud points as GT and sample the 100,000 points on our reconstructed mesh to calculate the metrics.

E More results

Here, we provide more visualization result. The high resolution visualization for the experiments from different types of input point clouds can be seen in Fig. 12, Fig. 13, Fig. 14. The high resolution visualization for the ablation study can be seen in Fig. 15 and Fig. 16.

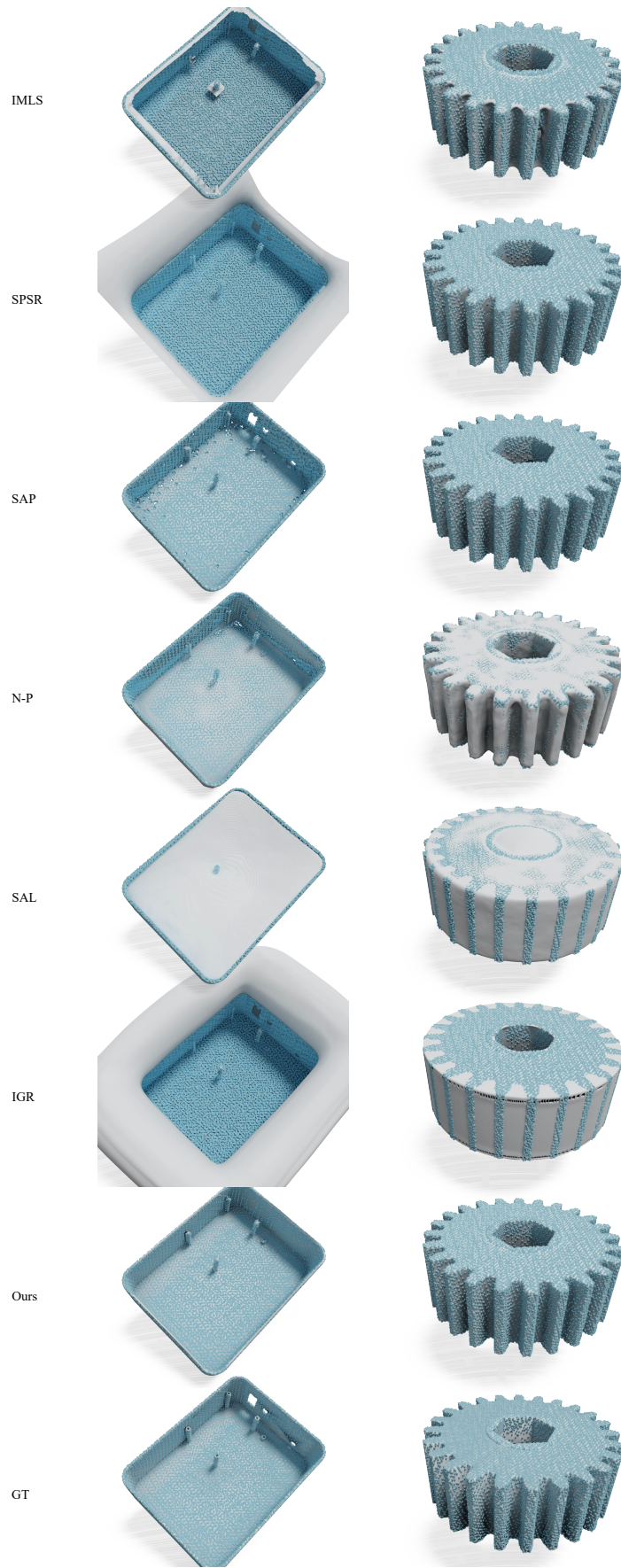


Figure 12: Visual comparison on the clean data.

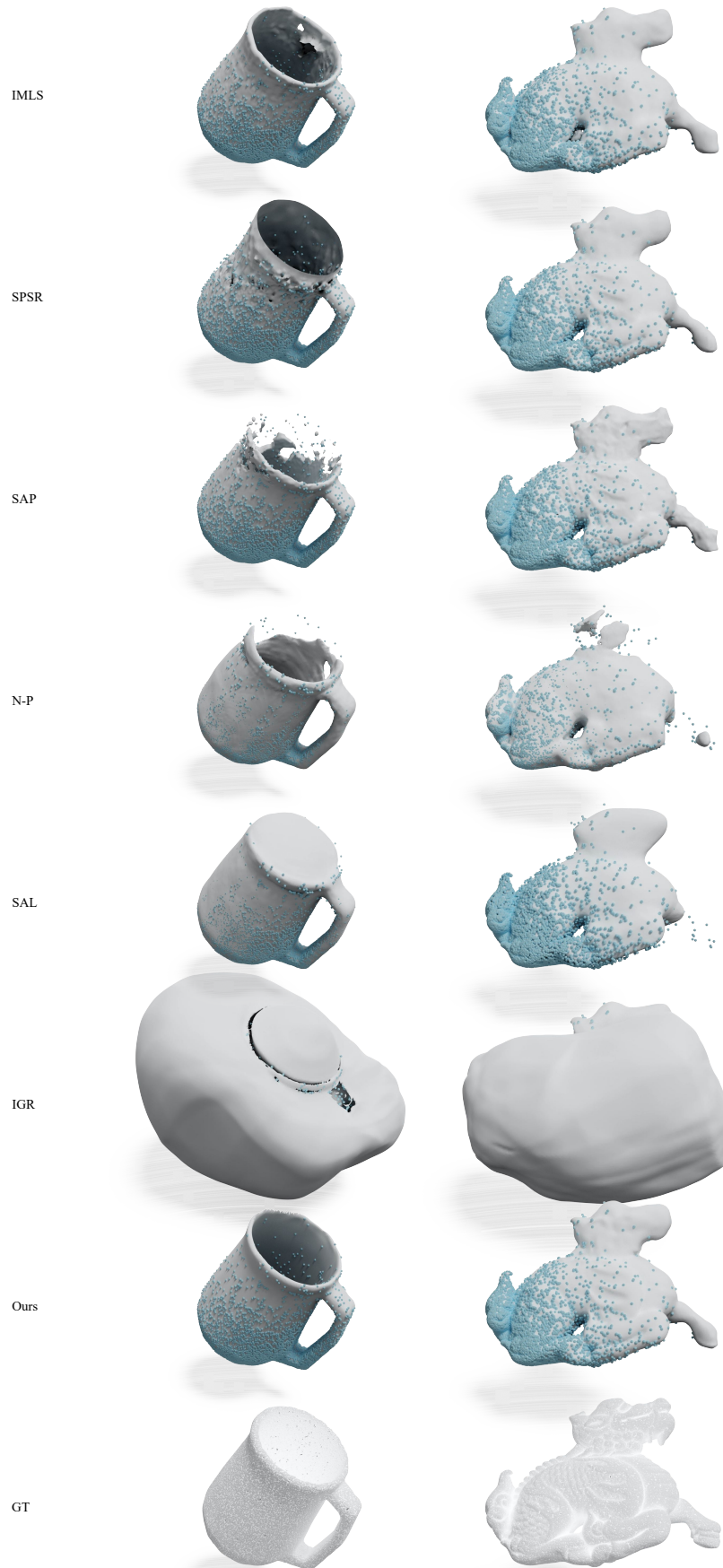


Figure 13: Visual comparison on the density-varying data.
16

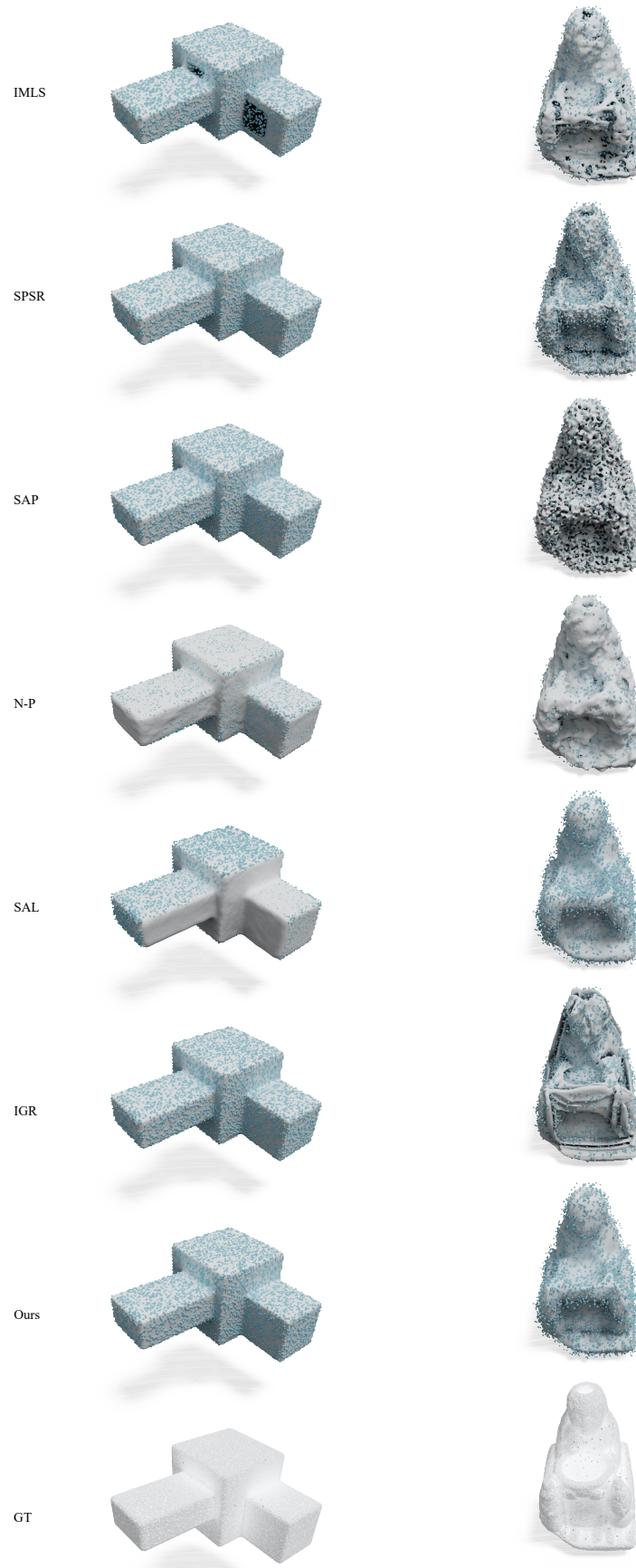


Figure 14: Visual comparison on noisy data.
17

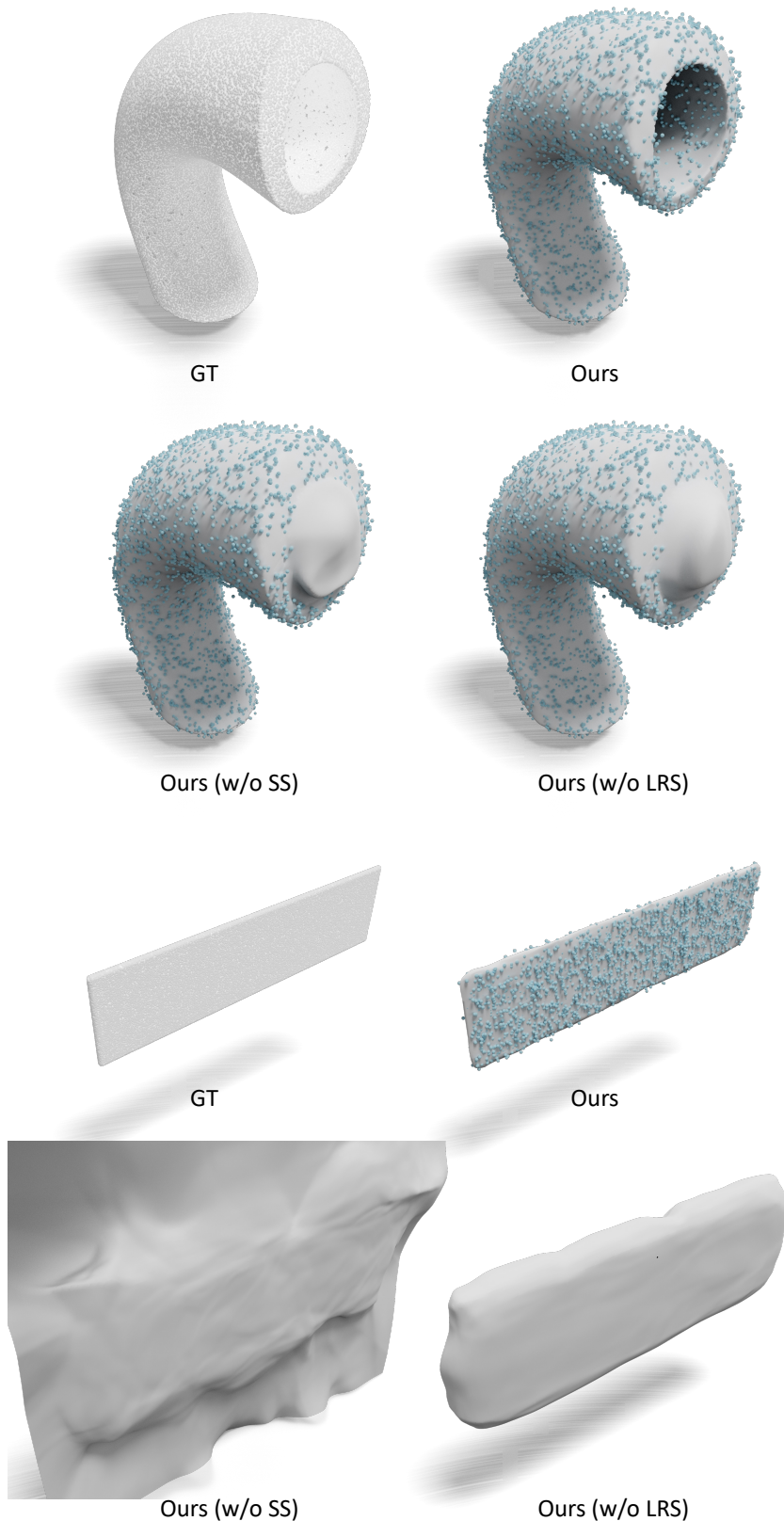
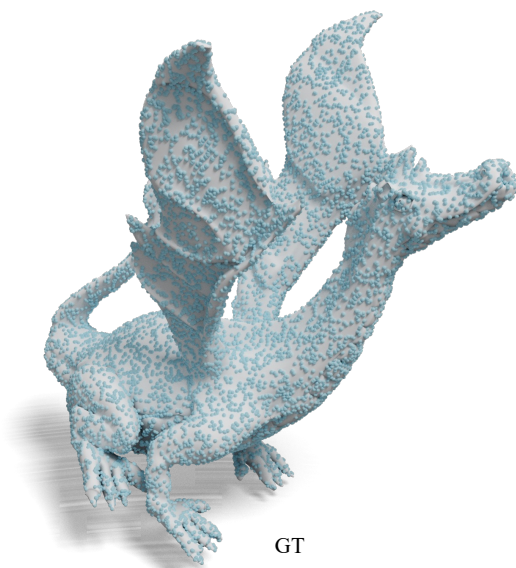
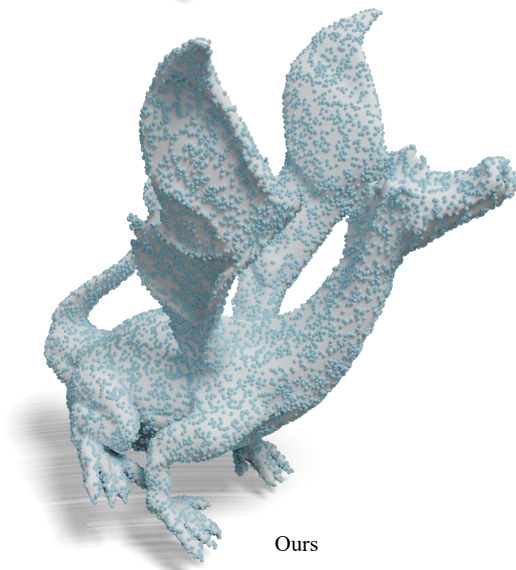


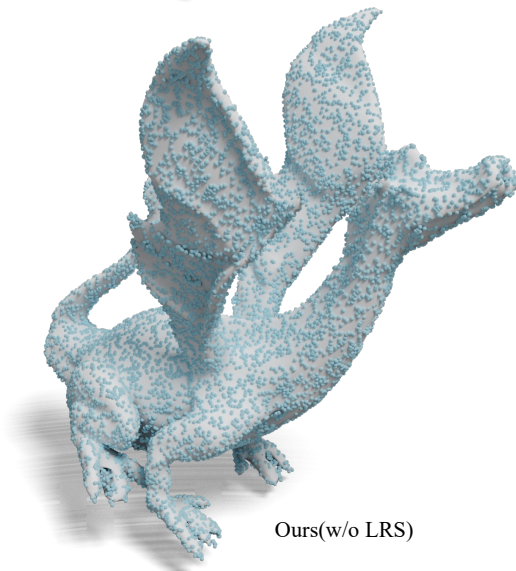
Figure 15: Visual comparison for the ablation study.



GT



Ours



Ours(w/o LRS)

Figure 16: Visual comparison for the ablation study.
19